Inorganic Chemistry

Forum Article

pubs.acs.org/IC

Six-Electron Reduction of Nitrite to Ammonia by Cytochrome *c* Nitrite Reductase: Insights from Density Functional Theory Studies

Dmytro Bykov*[,†] and Frank Neese*[,‡]

[†]qLEAP Center for Theoretical Chemistry, Department of Chemistry, Aarhus University, Gustav Wieds Vej 10A, DK-8000 Aarhus C, Denmark

[‡]Max-Planck Institut für Chemische Energiekonversion, Stiftstrasse 34-36, 45470 Mülheim an der Ruhr, Germany

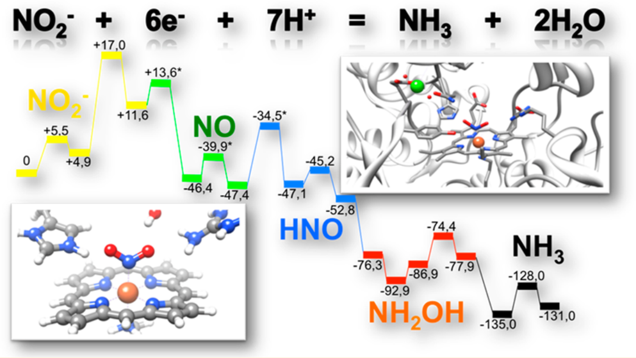

ABSTRACT: In this Forum Article, an extensive discussion of the mechanism of six-electron, seven-proton nitrite reduction by the cytochrome *c* nitrite reductase enzyme is presented. On the basis of previous studies, the entire mechanism is summarized and a unified picture of the most plausible sequence of elementary steps is presented. According to this scheme, the mechanism can be divided into five functional stages. The first phase of the reaction consists of substrate binding and N−O bond cleavage. Here His_{277} plays a crucial role as a proton donor. In this step, the N−O bond is cleaved heterolytically through double protonation of the substrate. The second phase of the mechanism consists of two proton-coupled electron-transfer events, leading to an HNO intermediate. The third phase involves the formation of hydroxylamine, where Arg_{114} provides the necessary proton for the reaction. The second N−O bond is cleaved in the fourth phase of the mechanism, again triggered by proton transfer from His_{277}. The Tyr_{218} side chain governs the fifth and last phase of the mechanism. It consists of radical transfer and ammonia formation. Thus, this mechanism implies that all conserved active-site side chains work in a concerted way in order to achieve this complex chemical transformation from nitrite to ammonia. The Forum Article also provides a detailed discussion of the density functional theory based cluster model approach to bioinorganic reactivity. A variety of questions are considered: the resting state of enzyme and substrate binding modes, interaction with the metal site and with active-site side chains, electron- and proton-transfer events, substrate dissociation, etc.

1. INTRODUCTION

1.1. Cytochrome *c* Nitrite Reductase (C*c*NiR). C*c*NiR is an important enzyme that is an indispensable part of the biological nitrogen cycle.[1,2] Specifically, C*c*NiR is an essential component of the dissimilatory nitrate reduction pathway to ammonia (DNRA). Several bacteria rely on the DNRA in order to grow anaerobically while using nitrate as the terminal electron acceptor.[3,4] The terminal step of the dissimilatory process is the reduction of nitrite to ammonia, which is catalyzed by C*c*NiR.[5] Importantly, the reduction can be carried out efficiently without the release of any potentially toxic intermediates.

C*c*NiR was isolated and crystallized for several bacteria: *Escherichia coli*,[6] *Wolinella succinogenes*,[7] *Sulfurospirillum deleyianum*,[8] *Desulfomonas desulfuricans*,[9,10] *Desulfovibrio vulgaris*,[11−13] and *Thioalkalivibrio nitratireducens*.[14,15] The crystallographic studies revealed C*c*NiR to be a homodimeric multiheme enzyme in all bacterial organisms except in the haloalkaliphilic bacterium *T. nitratireducens*.[14] The latter exists as a stable hexamer containing 48 hemes. The arrangement of the five hemes in the catalytic domain is, however, identical for all crystallographically characterized enzymes. The catalytic domain contains five covalently attached *c*-type hemes. Four heme irons are bis-histidine-ligated, while the fifth has a unique lysine as a proximal ligand. The bis-histidine-ligated hemes act as electron carriers, while the lysine-ligated iron is the active site of the protein. However, the C*c*NiR from *T. nitratireducens*[14] has an additional covalent bond between the active-site tyrosine and the adjacent cysteine. It also features product channels that open into the protein void interior space. Also, two six-coordinated calcium atoms are invariably present in the structure of C*c*NiR (Figure 1a,b).

The crystallographic investigations revealed that the active-site residues are strongly conserved in all periplasmic cytochrome *c* nitrite reductases (NrfAs) and form an environment of positive electrostatic potential around the active site.[16] Positions of the four bis-histidine heme groups in each monomer are strongly conserved. The distribution of the hemes in the protein facilitates fast and effective transfer of electrons to the active site.[17]

Special Issue: Small Molecule Activation: From Biological Principles to Energy Applications

Received: March 12, 2015
Published: August 3, 2015

DOI: 10.1021/acs.inorgchem.5b01506
Inorg. Chem. 2015, 54, 9303−9316

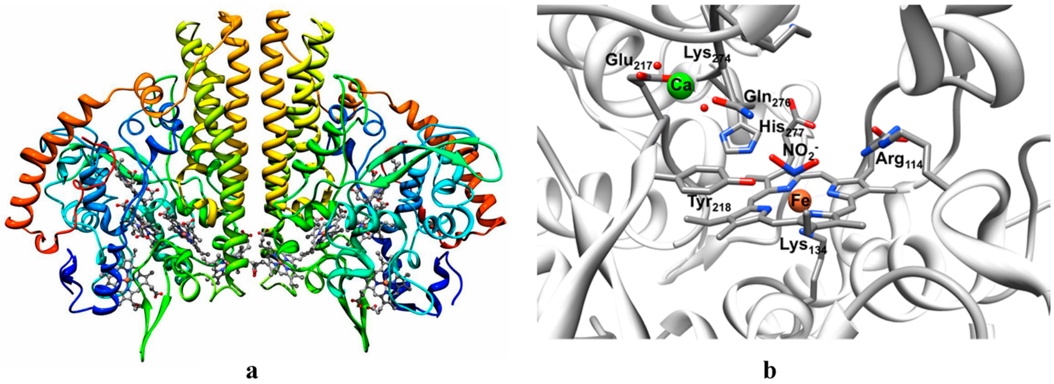

Figure 1. (a) Overall structure of *Cc*NiR. Shown is the functional dimer; each monomer contains five *c*-type hemes. (b) Active site of cytochrome *c* nitrite reductase (*Cc*NiR). The substrate occupies the distal position of the heme iron center. His_{277}, Tyr_{218}, and Arg_{114} form hydrogen bonds with the substrate. The Ca^{2+} coordination sphere is formed by Gln_{276}, Lys_{274}, Glu_{217}, Tyr_{218}, and two water molecules. Gln_{276} and Glu_{217} coordinate calcium through side-chain oxygen atoms (Gln_{276}-Oε1, Glu_{217}-Oε1, and Glu_{217}-Oε2), whereas Lys_{274} and Tyr_{218} provide main-chain carbonyl oxygen atoms (taken from the PDB structure 2E80).

The first reaction mechanism hypothesis was formulated in ref 18. The work reported the crystallographic analysis of several substrate complexes in combination with density functional theory (DFT) calculations of selected intermediates. The first stage of the proposed mechanism is the substrate binding and heterolytic cleavage of the first N−O bond. Two rapid reductions and a protonation step were proposed in order to reach a Fe^{II}−HNO intermediate. Further reduction by two electrons and protonation yield the hydroxylamine intermediate Fe^{II}−H_2NOH. The latter was crystallographically characterized.[19] The last stage is cleavage of the second N−O bond. The water molecule is released, and after reduction and protonation, the final product, ammonia, is formed.

*Cc*NiR reduces nitrite with high turnover rates (415−962 s^{-1}).[16] This suggests proton- (PT) and electron-transfer (ET) processes to be very effectively tuned by the protein. In particular, the number and spatial distribution of the electron-carrying hemes support effective ET to the active site. The Fe−Fe distances between the hemes never exceed 13 Å. Moreover, the monomers are interfaced through one of the ET hemes. Thus, efficient ET between the subunits can also be accomplished,[17] and the functional dimer already carries enough electrons for the entire reduction cycle. The electron supply between catalytic cycles is ensured by the formation of stable complexes with physiological redox partners [a membrane-associated complex with a membrane-anchored tetraheme cytochrome (NrfH) in the case of *W. succinogenes* *Cc*NiR[20] or with soluble pentaheme cytochrome NrfB in the case of *E. coli*[6]].

The second critical ingredient of the nitrite reduction process are protons. Protons are supplied through a positively charged substrate channel.[9] Importantly, the substrate channel contains a firmly bound calcium site in direct proximity to the active site (Figure 1b). It was also confirmed that calcium is essential for enzyme activity.[9,21] The role of Ca^{2+} in the substrate channel may be the structural stability of the active site combined with electrostatic interactions. Namely, the positive charge of the dication supports the inlet channel electrostatic potential, and the highly conserved coordination sphere stabilizes the protein conformation. The calcium site can also assist in proton-transport events. It is located only 10.7 Å away from the iron catalytic center. Thus, the water molecules in the inlet channel can dissociate, and the hydroxide ions can be effectively stabilized in the coordination sphere of the calcium ion, while protons take part in the catalytic nitrite reduction. Interestingly, the zinc-containing active site of carbonic anhydrase has a similar functionality.[22]

According to the widely accepted mechanistic hypothesis, the catalytic cycle commences by the splitting of the first N−O bond to create a ferrous heme nitrosyl intermediate. Heme nitrosyl derivatives have unique electronic structures and play an important role in biological processes.[23,24] Consequently, the nitric oxide reductase activity of *Cc*NiR was also studied for the enzyme from *E. coli*.[25] High turnover rates of 840 s^{-1} for NO were established, and a possible role of the enzyme as an NO detoxification agent was proposed. Additionally, the ferrous nitrosyl complex ($\{Fe(NO)\}^7$ in the Enemark and Feltham notation[26]) was extensively studied spectroscopically and kinetically as well as through DFT calculations.[27−30]

A number of model systems for the various intermediates of the reaction cycle have been synthesized and characterized.[31] Scheidt and co-workers extensively studied model complexes for the nitrite intermediate[32] and the nitrosyl intermediate in five-[33,34] and six-coordinated configurations.[35−38] Nitrosyl derivatives were also studied using theoretical methods[39,40] as well as in a combination of experimental techniques with DFT.[41,30]

Moreover, the reduction steps were experimentally investigated by protein film voltametry[42,43] and magnetic circular dichroism (MCD) spectroscopy.[44] It was speculated that the catalytic heme may act as a site for the coordinated exchange of two electrons;[45,46] the later MCD studies of *E. coli* NrfA did not support cooperative reduction.[44] More recently, several crucial catalytic issues were addressed: the nitrite binding kinetics and the role of distal histidine;[47] the proton-coupled electron-transfer (PCET) events;[48] pH-dependent reduction activation;[49] electron storage, distribution, and one-electron reduction processes.[50]

The hydroxylamine adduct, which is considered to be a terminal reaction intermediate, was characterized spectroscopically.[19] Furthermore, hydroxylamine is a known intermediate in a number of other enzymes.[51,52] These enzymes catalyzes the back-transformation of hydroxylamine into nitrite.

Despite the recent progress in the investigation of the reaction mechanism of *Cc*NiR by means of modern spectroscopic techniques, many details of the reaction mechanism remain experimentally inaccessible. To clarify the sequence of elementary chemical steps, modern theoretical methods can be of great utility. In particular, once it is established that theory is in agreement with the experimental facts for the known reaction intermediates, it can be used with some confidence to create a complete potential surface for the reaction consisting of structures and energies of all intermediates and the connecting transition states. For example, substrate activation by binding to the active site, proton and electron supply events, the first and second N–O bond cleavages, or dissociation of the final product ammonia must be considered in detail.

This paper is structured as follows. First, a short introduction of the computational methods is provided together with justifications for our choice of the actual computational model of the enzyme. Second, a summary of the computational results is provided. Third, several important questions in the modeling of the *Cc*NiR reaction mechanism are discussed. In particular, PT and ET events are addressed because of their importance for the six-electron, seven-proton nitrite reduction process.

1.2. Computational Methods in Studying Enzymatic Reactions. A wide spectrum of theoretical methods has been applied to study the enzymatic reactions. The simplest approach is based on classical molecular mechanics (MM).[53,54] Within this method, interactions between atoms are treated in the framework of Newtonian mechanics. The computational effort of the MM method is very low, which allows the study of entire proteins (several hundreds of thousands or even millions of atoms). This makes it possible to study conformational changes, protein–protein interactions, docking processes, etc. On the other hand, MM cannot provide information on the electronic structure of a given reaction intermediate and thus shed light on the processes like bond breaking, charge transfer, or electronic excitations.

A possibility to model intermediates in a reaction mechanism is given by applying a quantum mechanical (QM) method.[54] Using QM methods, a wealth of detailed information on the energetics, structural features, and electronic states can be received. Through computation of the spectroscopic parameters, a direct comparison with the experiment is possible.[55] Moreover, QM methods make predictions on the reactivity and thus the entire potential energy surface in the catalytic cycle of interest.[56] Unfortunately, the computational effort for QM methods is high. Depending on the method of choice, the formal scaling with the number of basis functions (proportional to the size of a molecule) is anywhere between $O(N^2)$ and $O(N^7)$.[57] While very promising linear scaling methods [$O(N)$ effort with respect to system size) are currently being developed, the majority of current applications faces the scaling problem. With the predominant DFT-based methodology, systems with about ∼300 atoms can be treated.

It is clear that a satisfactory QM treatment of entire proteins is currently still far out of reach. Hence, the majority of studies revert to a "cluster" approach. The essence of the method lies in the idea that the protein functionality can be modeled only using the active site together with the second coordination sphere.[58] The cluster approach is one of the most popular methods in computational chemistry nowadays in dealing with protein modeling.[59] The crucial question in the cluster approach is, what residues should be included in the model?

Obviously, a cluster model falls short of the real protein situation in a number of ways. Perhaps, the two most important shortcomings are (a) the lack of long-range electrostatic interactions and (b) the missing steric constraints of the protein environment. To incorporate the latter and prevent unrealistic residue movements in the course of a geometry optimization or transition-state search, it is customary to freeze a few α-carbon atoms to their crystallographic positions. To mimic missing protein influence, continuum solvation models are usually applied. One of the most popular continuum solvation models is COSMO.[60] In the vast majority of cases, the COSMO model gives reliable results in the computational studies of the protein reactivity if a low dielectric constant (ε = 4–8) is being used to model the protein matrix.[59] Another popular approach to deal with (a) and (b) is the combined QM/MM method. For further aspects of cluster versus QM/MM modeling approaches to enzymes, we refer to the work by Siegbahn and Borowski,[61] Liao and Thiel,[62] and Sumowski and Ochsenfeld.[63]

1.3. Computational Details. Starting structures for the enzyme active-site models were taken from the protein data bank[64] (PDB code 2E80[18]). Relying on the X-ray, voltammetry,[42] and mutational studies,[65,66] the model for the theoretical investigation was constructed in the following way: His_{277}, Arg_{114}, and Tyr_{218} were taken as the first-sphere distal ligands. These side chains were cut at α-carbon atoms. The heme is included in the model without its substituents. Lys_{134}, the proximal ligand of iron, was approximated by methylamine. Also, one crystallographic water molecule was included in the active-site model (Figure 2).

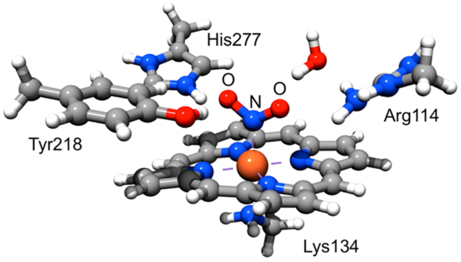

Figure 2. Computational model for the *Cc*NiR active site. The heme was modeled without its ring substituents; side chains His_{277}, Arg_{114}, Tyr_{218}, and Lys_{134} (taken from the pdb structure 2E80) were truncated at α-carbon atoms (these atoms were constrained during optimizations).

The calculations were performed with the ORCA electronic structure package, version 2.7,[67] using DFT.[58] The models of the enzyme active site were optimized with the BP86 functional[68,69] together with the resolution-of-the-identity (RI) approximation (in the Split-RI-J variant).[70] A triple-ζ basis set (TZVP),[71] together with a matching auxiliary basis set (TZV/J[72,73] in ORCA notation), was applied for all atoms. Subsequent numerical frequency calculations were performed for all models for the sake of verifying structures found as local minima and obtaining thermochemical corrections. Frequencies were computed through two-sided numerical differentiation of analytical gradients using increments of 0.002 bohr.

Single-point energy calculations were performed on the optimized structures with the B3LYP functional,[74,75] which is thought to provide higher accuracy than BP86 for reaction and activation energies.[59] The "chain-of-spheres" (RIJCOSX) approximation[76] was invoked in these calculations. The basis set was of triple-ζ quality with two sets of first polarization functions on all atoms [TZV(2d,2p)[77] in ORCA notation]. In order to crudely model the long-range dielectric effects of the protein, the COSMO[60] solvation model was employed with a dielectric constant of 4.9. All other COSMO parameters were left at their default values. Additionally, Grimme's DFT-D2 semiempirical correction was employed to account for dispersion forces, as implemented in the ORCA package.[78,79] It should perhaps be mentioned that these were valid choices for the computational constraints at the time that the work was conducted. With the present computational resources and modern algorithmic developments, slight adjustments to the protocol would be chosen, e.g., Grimme's more modern D3(BJ) correction,[80] a larger def2-TZVP basis set,[81] and the incorporation of scalar relativistic effects. However, the most pertinent conclusions of the study would not be changed by the choices made at the time.

The model structures and orbitals were visualized with the *Chimera* program.[82] The spin-restricted Kohn–Sham occupied orbitals were localized according to the Pipek–Mezey (PM) algorithm. The unoccupied orbitals are not localized. The spin-unrestricted Kohn–Sham orbitals were transformed into quasi-restricted orbitals[83] (QROs) and then localized with the PM algorithm.[84]

1.4. Calculation of the ET and PT Events in CcNiR.

1.4.1. Calculation of the Standard Redox Potentials and pK$_a$'s. In addition to the calculated free energy differences (protonation energies, electron affinities, and bond formation energies), it is convenient to analyze calculated pK_a values and redox potentials. The values of pK_a and redox potentials were estimated from the calculated free energy differences ΔG according to the following standard equations:

$$\Delta G_{\mathrm{PT}} = -RT \ln K_a \tag{1}$$

$$\mathrm{p}K_a = -\log K_a \tag{2}$$

$$\Delta G_{\mathrm{ET}} = -FE^\circ \tag{3}$$

where R is the universal gas constant, T the temperature, K_a the equilibrium constant, and F Faraday's constant. Inserting eq 2 into eq 1, one obtains a useful relationship between ΔG and pK_a:

$$\begin{aligned}\Delta G_{\mathrm{PT}} &= 2.303RT\,\mathrm{p}K_a \\ &= -1.37\ (\mathrm{kcal/mol}) \times \mathrm{p}K_a\ (\text{at } 298\ \mathrm{K})\end{aligned} \tag{4}$$

Equations 1 and 3 connect the absolute dissociation constant and redox potential with free energy changes in one proton/electron reaction. The most common way to find free energy changes is to apply a Born–Haber thermodynamic cycle. The method is widely used in pK_a and redox potential calculations of d metal complexes.[85] Using the Born–Haber cycle, ΔG_{PT} can be expressed:

$$\Delta G_{\mathrm{PT}} = \Delta G_g + \Delta G_{\mathrm{sol}}(\mathrm{A}^-) + \Delta G_{\mathrm{sol}}(\mathrm{H}^+) - \Delta G_{\mathrm{sol}}(\mathrm{AH}) \tag{5}$$

where ΔG_g is the free energy change of the AH deprotonation in the gas phase, ΔG_{sol} (A$^-$), ΔG_{sol}(AH), and ΔG_{sol} (H$^+$) are solvation free energies for AH, A$^-$, and a proton H$^+$. ΔG_{sol}(A$^-$) and ΔG_{sol}(AH) were calculated using COSMO, whereas the solvation free energy of a proton (275 kcal/mol) was taken from the literature.[86]

The Born–Haber cycle applied for the redox potential calculation gives the following equation for the free energy of the one-electron reduction:

$$\Delta G_{\mathrm{ET}} = \Delta G_g^{\mathrm{ET}} + \Delta G_{\mathrm{sol}}(\mathrm{OX}) - \Delta G_{\mathrm{sol}}(\mathrm{RED}) \tag{6}$$

where ΔG_g^{ET} is the free energy of the one-electron reduction in the gas phase and ΔG_{sol}(OX) and ΔG_{sol}(RED) are the solvation free energies of the oxidized and reduced forms, respectively. For the sake of comparison to experimental values, the absolute potential of the standard hydrogen electrode (SHE) should be added to the calculated values (the absolute electrode potential of SHE is 4.28 V according to Kelly et al.[87]).

Although the Born–Haber thermodynamic cycle is utilized frequently in pK_a and redox potential calculations, one must be aware that the ab initio prediction of pK_a values and redox potentials is exceedingly difficult. The redox potential of heme iron complexes is influenced by local charges, the ligand type, their basicity, and spatial alignment as well as more subtle effects like directed hydrogen bonds or nonplanar distortions. Unfortunately, the calculations also need to be of very high accuracy because an error of 1 kcal/mol in the calculated free energy translates to an error of approximately 40 mV in the predicted redox potential. Because the DFT methods that we use here have at least an error of 2–3 kcal/mol,[58] one cannot expect absolute errors of less than 100 mV in these calculations. Similar comments apply to the calculation of pK_a values. A number of strong local interactions such as hydrogen bonds, charge and dipole interactions, or interaction with the metal center in the protein environment can shift the pK_a values significantly.[88] However, because the active site does not undergo major structural changes throughout the reaction cycle, one may hope that the relative redox potentials and pK_a values are more accurate.

1.4.2. Calculation of the ET and PT Rates with DFT. According to Marcus theory (eq 7), the free energy of activation (ΔG^*) is related to the driving force of the ET step (ΔG°) and to the reorganization energy (λ) through the equation

$$\Delta G^* = \frac{(\lambda + \Delta G^\circ)^2}{4\lambda} \tag{7}$$

The reorganization energy can be expressed as a sum of the inner- (λ_{is}) and outer-sphere (λ_{os}) reorganization energies:

$$\lambda = \lambda_{\mathrm{is}} + \lambda_{\mathrm{os}} \tag{8}$$

where λ_{os} can be readily calculated by applying continuum theory as in the equation

$$\lambda_{\mathrm{os}} = (\Delta q)^2\left(\frac{1}{2r_1} + \frac{1}{2r_2} - \frac{1}{R}\right)\left(\frac{1}{D_{\mathrm{op}}} - \frac{1}{D_{\mathrm{s}}}\right) \tag{9}$$

Here Δq is the transferred charge, r_1 and r_2 are the effective radii of the reactants, R is the effective distance for ET, and D_{op} and D_{s} are the optical and static dielectric constants of the intervening medium. The D_{op} value is approximately 4 for a protein interior.[89]

The inner-sphere reorganization energy λ_{is} is a consequence of the geometric changes in the active site and heme donor to the configuration appropriate for ET. We used the procedure described in detail by Rosso and Rustad[90] to estimate the inner-sphere reorganization energy in the ET process. It was suggested that λ_{is} can be calculated from the total energy differences of four gas-phase clusters. Namely, λ_{is} consists of two components:

$$\lambda_{\mathrm{is}} = \lambda_{\mathrm{is1}} + \lambda_{\mathrm{is2}} \tag{10}$$

where λ_{is1} and λ_{is2} are

$$\lambda_{\mathrm{is1}} = E({\mathrm{Fe}^{\mathrm{III}}}_{\mathrm{Fe^{II}}}) - E({\mathrm{Fe}^{\mathrm{III}}}_{\mathrm{OPT}}) \tag{11}$$

$$\lambda_{\mathrm{is2}} = E({\mathrm{Fe}^{\mathrm{II}}}_{\mathrm{Fe^{III}}}) - E({\mathrm{Fe}^{\mathrm{II}}}_{\mathrm{OPT}}) \tag{12}$$

Here E denotes the total electronic energy and the subscript "OPT" indicates the minimum energy structure; ${\mathrm{Fe}^{\mathrm{III}}}_{\mathrm{Fe^{II}}}$ represents a single-point energy of the $\mathrm{Fe^{III}}$ active site in the optimized $\mathrm{Fe^{II}}$ geometry and vice versa for ${\mathrm{Fe}^{\mathrm{II}}}_{\mathrm{Fe^{III}}}$.

The inner-sphere reorganization λ_{is} term for PCET and PT was calculated according to the theory developed by Hammes-Schiffer et al.[91] The inner-sphere reorganization energy, assumed to originate from the calcium-site−ligand bond reorganization and Fe−N−O core reorganization, is approximated as

$$\lambda_{\mathrm{is}} = \sum_j \frac{f_j^{\mathrm{r}} f_j^{\mathrm{p}}}{f_j^{\mathrm{r}} + f_j^{\mathrm{p}}} (\Delta q_j)^2 \tag{13}$$

where the summation runs over calcium−ligand modes (these modes were chosen as metal−ligand bonds of the calcium coordination sphere), Fe−N(NO) and N−O(NO) modes, f_j^{r} and f_j^{p} are the equilibrium force constants of the jth mode in the reactant and product, respectively, and Δq_j is the difference between the reactant and product equilibrium bond lengths. The force constants were calculated at the BP86/TZVP level of theory according to a procedure developed by Petrenko et al.[92]

2. RESULTS AND DISCUSSION

2.1. Substrate Binding and Activation in CcNiR.

2.1.1. Substrate Binding. Spin State of the Porphyrine Iron. As a model of the enzyme resting state, $\mathrm{Fe{-}H_2O}$ and $\mathrm{Fe{-}OH^-}$ complexes were considered. The substrate nitrite coordination through nitrogen and oxygen was probed. Because the His_{277} active-site ligand can occur in protonated and deprotonated forms under physiological conditions, both possibilities were taken into consideration.

The axial ligand's role in the energetics and reactivity of hemoproteins is a longstanding issue. Rydberg et al.[93] provide an extensive overview of the geometric and electronic structure, spin-state energetics, bonding, and reaction energies for intermediates in catalysis by cytochrome P450, peroxidase, and catalase. The ferric water complexes were concluded to be unstable, and the ferric hydroxyl low-spin state is much more stable than the higher spin states, in contradiction with experimental results.[94] It should be noted that pure functionals always overestimate the stability of the lower spin states, while the hybrid functionals perform generally better.[95] Although there is no single functional that is capable of accurately predicting the metal oxidation and spin states for a large variety of complexes, the B3LYP hybrid functional employed here is among the better ones in this respect. Moreover, in addition to B3LYP, the B3LYP* functional was used. B3LYP* differs from B3LYP by the amount of Hartree−Fock exchange (15% vs 20%). B3LYP* is known to give reasonable results for a variety of transition-metal complexes.[96]

According to our results, low-spin ferrous and ferric hydroxo complexes are 8 kcal/mol lower in energy than the respective triplet and quartet states. The high-spin quintet and sextet forms are even more unfavorable. The results with the B3LYP* functional show the same trend. The low-spin state is separated by 9.2 (10.5) kcal/mol from the triplet (quartet) states and by 12.8 (14.7) kcal/mol from the quintet (sextet) states. In the calculations with a protonated His_{277} side chain, the $\mathrm{OH^-}$ group receives a proton from His_{277} and rebinds to the metal center as an axial ligand.

Resting State of the CcNiR Enzyme. The axial water ligand is only weakly bound to the metal center. The binding energies of −10.8 and −5.6 kcal/mol were found for the ferrous and ferric complexes, respectively.[97] The bond distance between the catalytic iron center and the oxygen of the bound water is 2.106 Å. This value is in good agreement with the Fe−O distance of 2.1 Å determined from the X-ray structure of Einsle et al.[18] A low-spin ferric iron with a ligated water molecule is assumed to represent the enzyme resting state.

The reduction to the ferric form immediately leads to an increase in the Fe−O distance up to 2.134 Å. The Fe−O bond is weakened, and thus the axial water can be easily displaced by the nitrite. The driving force was found to be −39 kcal/mol for substitution of the bound water by nitrite.

Nitrite Binding in the Active Site of the Enzyme. The nitrite substrate can bind through oxygen or nitrogen. Although in the investigation of Einsle et al.[18] the binding was found to take place through a nitrogen atom, there is other evidence that oxygen-type binding is also possible. For instance, the oxygen-type binding was studied for horse-heart myoglobin by Yi et al.[98] The horse-heart myoglobin is like CcNiR and has an iron porphyrin active site, but the proximal site is occupied by a histidine axial ligand. The authors concluded that the oxygen-type binding is possible because of the formation of a specific hydrogen bond in the active-site pocket. Our theoretical results imply that oxygen coordination is intrinsically unfavorable (the difference in the nitrogen- and oxygen-type binding energies is larger than 4 kcal/mol). Nevertheless, the nitrogen binding is only slightly more favorable, thus making it possible to stabilize the oxygen binding with additional strong hydrogen bonding. The bond distances calculated for the $\mathrm{Fe{-}O(NO_2)}$ complex are elongated compared to those for the $\mathrm{Fe{-}N(NO_2)}$ motive, and thus the substrate ligand is only very weakly bound.

Substrate Back-Bonding in the Ferrous Nitrite Complex. The most important distinct feature of the nitrogen-bound ferrous nitrite complex is the back-bonding effect. The effect reveals itself in an interaction of the low-lying metal d orbital and the lowest unoccupied molecular orbital (LUMO) of the nitrite molecule (Figure 3). As a consequence, the ferrous nitrite complex is energetically most favorable and exhibits a short $\mathrm{Fe{-}N(NO_2)}$ bond distance (1.877 Å). Additionally, the back-bonding activates the substrate by pushing the electron density from the iron to nitrite LUMO, which has π-antibonding character with respect to the N−O bond.

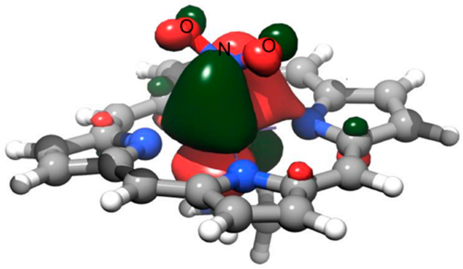

Figure 3. Back-bonding interaction of the nitrite molecule with ferrous iron. The d_{xz} orbital of iron interacts with the LUMO of the $\mathrm{NO_2}^-$ molecule, which has antibonding character with respect to the N−O bond.

The back-bonding effect in ferrous nitrite model complexes was discussed extensively.[32,99,31] It was also indicated that the spatial orientation of the nitrite relative to the porphyrin plane is also diagnostic of the back-bonding effect.[31] In addition, the nitrite orientation was investigated experimentally. The data from the Mössbauer and electron paramagnetic resonance experiments[100] suggest the orientation where the plane of the metal d-bonding orbital is perpendicular to the nitrite plane. Thus, the π-acceptor capabilities of the substrate molecule are maximized. The theoretical investigation[97] suggests the same orientation (Figure 3).

2.1.2. N–O Bond Cleavage. Possible Pathways for the First N–O Bond Cleavage Based on Protonated His_{277}. The pK_a of the histidine side chain is close to 7, which implies that both forms, protonated and deprotonated, are possible under physiological conditions. Thus, taking His_{277} in the doubly protonated form, each of the active-site side chains, His_{277}, Arg_{114}, or Tyr_{218}, could provide a proton for the first reaction step. All three possibilities were studied. The results imply that Tyr_{218} cannot be effective as a proton donor in this phase of the reaction. Furthermore, the HONO adduct is unstable in the case when Tyr_{218} acts as a proton donor. Stable HONO is formed when His_{277} or Arg_{114} is a proton donor. These two reactions differ significantly in their ΔG value. The reaction with Arg_{114} is significantly endothermic by +17.7 kcal/mol, whereas protonation from His_{277} has ΔG = +4.9 kcal/mol and is, hence, energetically more feasible. Also, the transition-state energy was found to be only +5.5 kcal/mol.

For the N–O bond to be cleaved, the second proton must be transferred to the HONO adduct. Again, the second proton may be coming from one of the three active-site side chains: Arg_{114}, Tyr_{218}, or His_{277}. Obviously, His_{277} must be reprotonated first. All three possible scenarios were studied computationally. It was found that, regardless of the pathway, the second PT is highly endothermic. Moreover, the allocated transition-state complexes are energetically hard to reach. According to experimental kinetics studies,[17,21] the barrier of the rate-limiting step should not exceed 15.2 kcal/mol. Analysis of all options shows that the most probable pathway for N–O bond cleavage is endothermic His_{277} reprotonation and subsequent PT over a barrier of +12.1 kcal/mol. The water molecule dissociates from the substrate, and $\{Fe(NO)\}^6$ is formed.

Possible Pathways for the First N–O Bond Cleavage Based on Deprotonated His_{277}. The other alternative pathway may occur when the His_{277} side chain is deprotonated. In this case, possible scenarios are (1) transfer of a proton from Tyr_{218}, (2) transfer of a proton from neutral His_{277}, and (3) transfer of a proton from Arg_{114}. Both options (1) and (2) were found to be thermodynamically highly endothermic. Option (3) can be realized in two possible ways. The first way is direct PT from Arg_{114}, and the second is via an intermediate water molecule. It was found that both reactions are very similar in energy (the difference is only ~0.3 kcal/mol, which is insignificant within the error limits of the employed DFT methodology). Hence, both routes may be feasible. The activation energy was found to be +16.7 kcal/mol. When this value is compared with the one experimentally found,[17,21] it is clear that the values are very close. Therefore, a conclusion that both side chains may act as proton donors on this stage can be drawn.

To complete the N–O bond cleavage, an extra proton must be supplied to the substrate. Again, two possibilities must be considered. The first is the transfer from Tyr_{218}, and the second is Arg_{114} reprotonation and then transfer to the substrate. The transfer from Tyr_{218} was found to be unfeasible because both the reaction enthalpy (+19.2 kcal/mol) and the transition-state energy (+31.1 kcal/mol) are too high. On the contrary, the reprotonation of Arg_{114} was estimated to be exothermic by −13 kcal/mol, and the reaction barrier of +14.1 kcal/mol was found. This makes the reprotonation pathway the most probable.

Summary of the N–O Bond Cleavage. Additional insight into the mechanism of N–O bond cleavage may be obtained from geometrical and electronic structure analysis of the HONO adduct and the transition state. For the HONO adduct, a large negative charge of −0.72 (Mulliken population analysis) was found for the hydroxyl oxygen, whereas the other oxygen bares only a charge of −0.2. The nitrogen in HONO is positively charged (+0.40). Thus, the N–OH bond is strongly polarized. Also, this bond is elongated. As for the transition-state complex geometry, the N–OH bond length is even more elongated up to 2.21 Å. Basically, the N–OH bond is already cleaved and the proton donated from the Arg_{114} side chain interacts with the lone pair formed on the hydroxyl oxygen. Thus, analysis shows that N–O bond cleavage is heterolytic, which is also consistent with previous investigations.[18,101]

2.2. Heme Iron Nitrosyl Intermediates. *2.2.1. Introducing the Notation for the Iron Nitrosyl Derivatives in CcNiR.* To keep track of different nitrosyl-derived intermediates after the first N–O bond cleavage, the following notation is used: the current adduct is shown in parentheses; the number and distribution of the protons in the active site are denoted by letter H with the according subscript. For example, the complex shown in Figure 4 will be just denoted as (NO). It represents the $\{Fe(NO)\}^6$ core configuration with no additional protons on the three active-site side chains. Protonation of (NO) would lead to $(NO)H_T$, where Tyr_{218} is protonated. $(NO)H_TH_A$ denotes both Tyr_{218} and Arg_{114} to be in the protonated state. The fully protonated complex $\{Fe(NO)\}^6$ is $(NO)H_TH_AH_H$. The reduction of the $\{Fe(NO)\}^6$ complex leads to formation of the paramagnetic $\{Fe(NO)\}^7$ species, which in our notation is denoted as (NO*). Again, taking into account protonation of the side chains, four intermediates are possible: (NO*), $(NO^*)H_T$, $(NO^*)H_TH_A$, and $(NO^*)H_TH_AH_H$. Further reduction leads to the $\{Fe(NO)\}^8$ complex. This state is also considered in four protonation states: (NO^-), $(NO^-)H_T$, $(NO^-)H_TH_A$, and $(NO^-)H_TH_AH_H$. Additionally, the formation of HNO-based adducts (HNO*), $(HNO^*)H_T$, $(HNO^*)H_TH_A$, and $(HNO^*)H_TH_AH_H$ is considered.

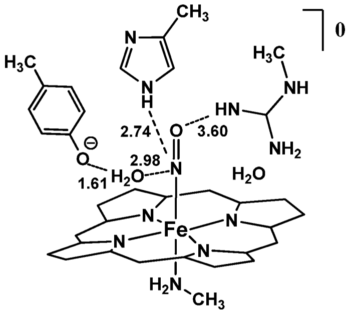

Figure 4. Starting structure for the investigation of the series $\{Fe(NO)\}^6$–$\{Fe(NO)\}^8$.

Obviously, an important question here is the order of the active-site side-chain protonation events. Because the protonation is governed by the acidities of the corresponding side chains and those are strongly dependent on the protein surrounding the environment, the *PROPKA3.1* program was used.[102−104] PROPKA allows calculation of the pK_a values within the protein interior. Our results with PROPKA showed that the most basic residue in the active site for all crystal structures is Tyr_{218}. The estimated pK_a is 14−15. For Arg_{114}, the pK_a value is 12−13. His_{277} was found to be very acidic with a pK_a value of about 1−2. In accordance with pK_a predictions, protonation of the active-site side chains happens in the following order: first Tyr_{218}, then Arg_{114}, and finally His_{277}.

2.2.2. Electronic Structure and Bonding in the Series {Fe(NO)}^{6}−{Fe(NO)}^{8}. Because the nitrosyl's electronic structure was extensively discussed in the literature,[105,106,38] the focus of this section is on the electronic structure changes caused by interaction with the active-site side chains.

For the low-spin {Fe(NO)}^{6} complexes (NO), (NO)H_T, (NO)H_TH_A, and (NO)$H_TH_AH_H$, the electronic structure is the Fe^{2+} metal center bound to a closed-shell NO^+ ligand.[23] The orbitals from the t_{2g} set are doubly occupied. One of them is a d_{xy}-based nonbonding orbital, and two others are formed from metal d_{xz} and d_{yz} interacting with NO−π^* fragment orbitals (Figure 5a). These two orbitals have π-bonding character with respect to the metal−N(NO) bond. LUMO and LUMO+1 are strongly antibonding with respect to both the Fe−N(NO) and N−O bonds.

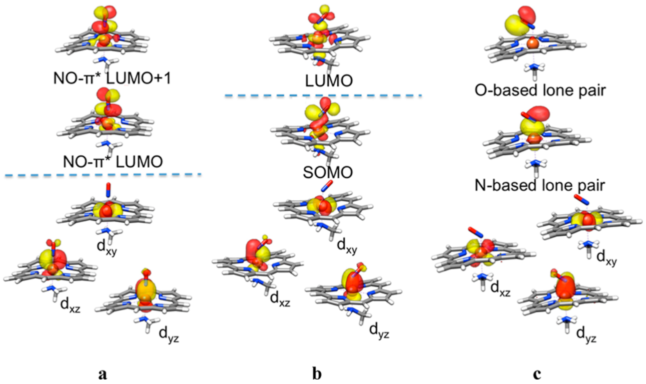

Figure 5. Important MOs calculated using the B3LYP/TZV(2d,2p) level of theory. Active-site side chains are omitted for simplicity. (a) {Fe(NO)}^{6} MOs are presented. The occupied orbitals were localized according to the PM algorithm. (b) {Fe(NO)}^{7} MOs are depicted. The spin-unrestricted Kohn−Sham orbitals were transformed into QROs and then localized with the PM algorithm. (c) {Fe(NO)}^{8} MOs are considered.

The interaction with the surrounding side chains is mainly due to polarization of one of the NO−π^*-based molecular orbitals (MOs). This polarization may become rather strong because {Fe(NO)}^{6} complexes are strong electrophiles.[31] Thus, the oxygen (Tyr_{218})-based lone pair interacts with the NO−π^*-based LUMO. The result of the interaction is bond weakening and elongation because the LUMO has antibonding character with respect to both the Fe−N(NO) and N−O bonds. In addition, quasi-degeneration of NO−π^*-based orbitals is disturbed, causing bending of the Fe−N−O unit. Upon protonation, a strong repellent effect between the side chains and NO is observed because of the positive charge on the nitrosyl.

Reduction {Fe(NO)}^{6} leads to {Fe(NO)}^{7}. The unpaired electron is placed in the nearly degenerate set of strongly antibonding Fe−NO orbitals with mainly NO−π^* character. The Fe−N−O unit is bent as a result of the Jahn−Teller effect. As a consequence, two NO−π^*-based orbitals formed. The first is a π^*_σ singly occupied molecular orbital (SOMO), which has σ-bonding character with respect to the Fe−N(NO) bond. The second is a π^*_π antibonding LUMO (Figure 5b). The pronounced stability of the Fe−NO bond in the {Fe(NO)}^{7} complex[106] is due to the fact that the SOMO has σ-bonding character with respect to the Fe−N(NO) bond. The shape and composition of the SOMO has been the subject of much debate in the literature.[107] A conclusion has been drawn that, in this specific case, pure functionals give better results than hybrid functionals.[108]

In contrast to the stability of the Fe−NO bond, the N−O bond of the NO ligand is weakened. The reduction {Fe(NO)}^{6} to {Fe(NO)}^{7} was found to be ligand-centered for atomic charge analysis. The charge of the iron atom changes by only 0.01 e^- upon reduction, while the charge on the NO fragment becomes more negative by 0.25 e^-. For the series (NO*)-(NO*)$H_TH_AH_H$, a gradual increase of the positive charge of the second-sphere residues leads to Fe−N(NO) bond elongation and Fe−N(Lys_{134}) bond shortening. The reasoning is that the electron density flow from the iron porphyrin fragment to the NO ligand influenced by the positive charge of the surrounding residues.

The {Fe(NO)}^{8} core is formed upon further reduction. {Fe(NO)}^{8} is best described as a mixture of Fe^{II}−NO^- and Fe^I−NO resonance structures. Here, the t_{2g}-derived orbitals essentially have the same character as those in {Fe(NO)}^{6} and {Fe(NO)}^{7}. Namely, one nonbonding MO and two π-bonding MOs are in the t_{2g} set. The addition of an electron leads to double occupation of the π^*_σ orbital. Thus, the Fe−NO bond is further elongated. The N−O double bond is split, and two lone pairs on nitrogen and oxygen are formed (Figure 5c). The lone pairs at the NO nitrogen are possible targets of electrophilic attack of incoming protons. Also, because the π^*_σ orbital in {Fe(NO)}^{8} does not have a strong antibonding effect with respect to the N−O bond, the latter becomes stronger. This strengthening is also discussed in the literature by Lehnert et al.[109] The shift of the N−O stretching frequency to 1500 cm^{-1} from 1290 cm^{-1} for a free NO^- molecule was found.

Analysis of the interaction with the surrounding side chains reveals an interesting effect. Hydrogen bonding with O(NO) makes the NO−π^* orbital more populated, and as a consequence, the Fe−N(NO) bond is strengthened, while the N−O bond is weakened. The effect is different when hydrogen bonding is established with N(NO). In this case, both the Fe−N(NO) and N−O bonds are weakened as the electron density is transferred into a (partial sp^2) nitrogen-based nonbonding orbital. The effect was also revealed in the investigation of Xu and Spiro.[110]

The electronic structures of (HNO*)H_T and (HNO*)H_TH_A were also considered. Interestingly, the electronic structures resemble that of the {Fe(NO)}^{8} series rather than {Fe(NO)}^{7}. A lone pair on oxygen is formed. The other lone pair on N(NO) is engaged in a bond with hydrogen-forming HNO. Moreover, the SOMO in both the (HNO*)H_T and (HNO*)-H_TH_A complexes is almost purely (93.3%) iron-based. Thus, the electronic structure can best be described as a low-spin Fe^{III} center with neutral HNO species bound to it. Further reduction leads to (HNO^-)H_T and (HNO^-)H_TH_A complexes ({FeHNO}^{8} core). The electronic configuration of the

$(\mathrm{HNO^-})\mathrm{H_T}$ and $(\mathrm{HNO^-})\mathrm{H_TH_A}$ complexes can be described as low-spin $\mathrm{Fe^{2+}}$ with HNO.

2.2.3. ET and PT Reaction Energetics. Having discussed the electronic structure and bonding in the series $\{\mathrm{Fe(NO)}\}^6$–$\{\mathrm{Fe(NO)}\}^8$, we are now in a position to study the energetic aspects of the recharging of the active site, i.e., the energetics of the consecutive proton and electron addition to the active site of the protein. Figure 6 summarizes the energetics of possible protonation and reduction reactions. To construct the scheme, an adiabatic electron affinity of 94 kcal/mol and the proton absolute hydration enthalpy from cluster-ion solvation (−275 kcal/mol)[86] were used as reference values.[111] The scheme contains protonation energies, electron affinities, and bond formation energies, as well as calculated pK_a values and redox potentials. These values were estimated from the free energy differences ΔG using equations presented in section 1.4.1.

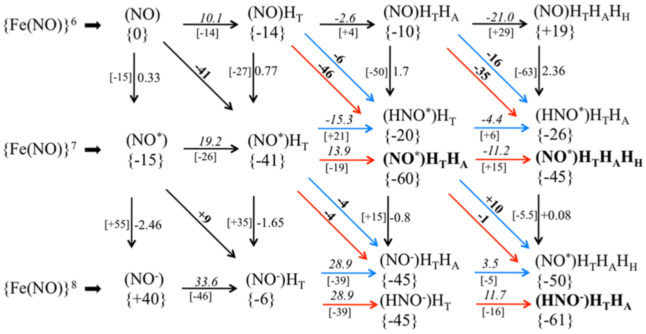

Figure 6. Overall energetics of the recharging process based on ref 111. The complexes in the first row correspond to $\{\mathrm{Fe(NO)}\}^6$, second row $\{\mathrm{Fe(NO)}\}^7$, and third row $\{\mathrm{Fe(NO)}\}^8$. There are free energy changes (ΔG in kcal/mol) in the square brackets and relative energies with respect to the initial (NO) complex in the curved brackets. All energies are obtained using B3LYP-D2/TZV(2d,2p). Calculated pK_a values (in italics) for the protonation reactions are located above the horizontal arrows. The redox potentials (in V) for reduction reactions are placed on the right of the vertical reaction arrows. Formation free energy changes (in kcal/mol) for PCET reactions are in boldface. Red arrows denote reactions where a proton moves to a side chain, while blue arrows highlight reactions when a proton is transferred to the NO ligand. In the case where two complexes have the same number of protons, the complex that has a lower relative energy is highlighted in bold and is taken as the starting point for the consecutive reactions.

Energetics analysis using the thermodynamic data from Figure 6 revealed two possible reaction pathways: (1) two consecutive PCET reactions $[(\mathrm{NO})\mathrm{H_T} \rightarrow (\mathrm{NO^*})\mathrm{H_TH_A} \rightarrow (\mathrm{HNO^-})\mathrm{H_TH_A}]$ and (2) reduction $[(\mathrm{NO})\mathrm{H_T} \rightarrow (\mathrm{NO^*})\mathrm{H_T}]$ followed by PCET $[(\mathrm{NO^*})\mathrm{H_T} \rightarrow (\mathrm{NO^-})\mathrm{H_TH_A}/(\mathrm{HNO^-})\mathrm{H_T}]$ and protonation $[(\mathrm{NO^-})\mathrm{H_TH_A} \rightarrow (\mathrm{HNO^-})\mathrm{H_TH_A}/(\mathrm{NO^-})\mathrm{H_TH_AH_H}]$. In the case of the $(\mathrm{NO^-})\mathrm{H_TH_AH_H}$ complex, reaction proceeds further through abstraction of a proton from His_{277} or Arg_{114} and formation of the $(\mathrm{HNO^-})\mathrm{H_TH_A}$ product. It should be noted that the second pathway may be beneficial because it contains a series of consecutive steps with small energetic effects, which is an advantage under the conditions of a living cell. Nevertheless, the actual reaction pathway is chosen by the overall kinetics of the process.

2.2.4. Modeling of the Proton Supply in the CcNiR. One of the *Cc*NiR integral structural and functional sites is the calcium site. The calcium site is a part of the inlet channel. It is located close to the catalytic active site, playing an important role in the protein reactivity. The first important role of the calcium site is the structural element role, as was discussed by Cunha et al.[9] The second role is maintenance of the inlet positive charge. The substrate nitrite is negatively charged; thus, the inlet channel must bear positive residues. A calcium dication in direct proximity to the active site thus attracts the nitrite molecule to the active site. Also, the calcium site was proposed to modulate the proton supply process.[111] In this case, the calcium site acidifies the coordinated water molecules. Thus, the water molecules can dissociate easily, supplying the protons to the active site, whereas the hydroxyls stay affectively bound in the calcium coordination sphere. This study was conducted using a model of a part of the inlet channel depicted in Figure 7. To construct the model, residues within 6 Å from the central calcium cation were included. Thus, residues of the first-coordination-sphere ligands were added in the modeling. Also, Tyr_{255}, Tyr_{219}, Tyr_{218}, Trp_{391}, Leu_{273}, and Ala_{275} residues were included, finalizing the complete hydrogen-bonding network around the calcium site. Using this model, one can obtain realistic adiabatic proton affinity reference values and thus estimate the energetics of the protonation reactions. Also, the reorganization energy for the PT reactions can be estimated.

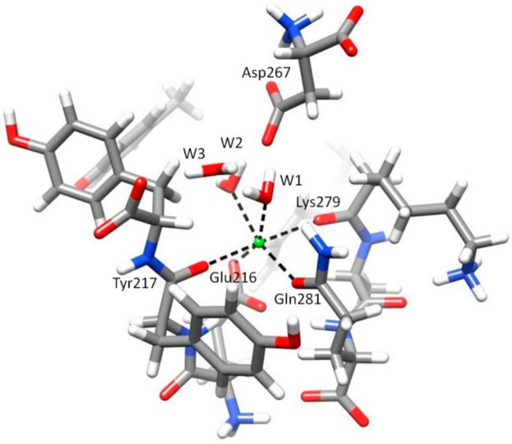

Figure 7. Optimized structure of the calcium-site model, representing part of the inlet channel. The model comprises residues within 6 Å from the central atom. A total of 170 atoms are included in the model. In both models, W1 stands for the water molecule that is protonated/ionized in the investigation.

The proton affinity for the calcium-site model was found to be −269 kcal/mol. It is important to compare this number with the solution reference value of −275 kcal/mol.[86] The difference of ~6 kcal/mol means that the thermodynamic driving force for the protonation reactions during the entire turnover is getting larger in the presence of the calcium site. This may be the proton supply role of the calcium site in the *Cc*NiR enzyme.

Also, the calcium site has two water molecules in the coordination sphere. It was found that ΔH of dissociation for the bound water and water in solution is significantly smaller. Therefore, it was postulated that the calcium site may act as an acid/base catalytic subunit.[111] The protons from the dissociated coordinated water molecules can be directly transferred to the active site because the substrate molecule is only few angstroms away from the calcium coordination sphere.

2.2.5. Analysis of the Kinetic Barriers. Estimations of the kinetic barrier heights were carried out within the Marcus theory framework. Section 1.4.2 contains all formulas needed for the computations.

The outer-sphere reorganization energy of 11 kcal/mol was calculated by taking an optical dielectric constant equal to 2. For the inner-sphere reorganization energy, values ranging between 16 and 37 kcal/mol were found. Comparing this values to the measured cytochrome *c* self-exchange reorganization energy[112] gives good agreement. Using the same framework, PCET and PT reactions were estimated to have reorganization energies of 27 and 12 kcal/mol, respectively. On the basis of the total reorganization energies (the sum of the inner and outer parts), adiabatic barriers were estimated and found to vary significantly. A graphical representation of the results is shown in Figure 8. For example, the reaction $(NO)H_TH_A \rightarrow (NO^*)H_TH_A$ is effectively barrierless, whereas $(NO^*) \rightarrow (NO^-)$ has an estimated barrier of 58 kcal/mol. It should, however, be noted that the extreme examples from above are never reached under normal conditions. Instead, two possible pathways proposed earlier from the thermodynamic analysis proceed only through moderate barriers. The pathway (1) has two consecutive PCET reactions $[(NO)H_T \rightarrow (NO^*)H_TH_A \rightarrow (HNO^-)H_TH_A]$ with estimated activation barriers of 2 and 6.5 kcal/mol, respectively. The pathway (2) is the reduction $(NO)H_T \rightarrow (NO^*)H_T$ with an activation energy of 2 kcal/mol, followed by the PCET $(NO^*)H_T \rightarrow (NO^-)H_TH_A/(HNO^-)H_T$ with a barrier of 5 kcal/mol and almost barrierless (0.1 kcal/mol) protonation $(NO^-)H_TH_A \rightarrow (HNO^-)H_TH_A/(NO^-)H_TH_AH_H$ (Figure 8).

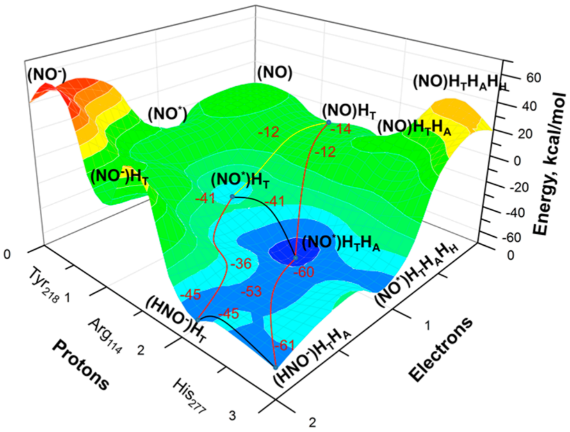

Figure 8. Nitrosyl intermediate energetics in the reaction cycle of *Cc*NiR. The scheme is based on the results from ref 111. Feasible steps are highlighted with curved lines (red for PCET, yellow for ET, and black for PT).

A closer analysis of the estimated kinetics reveals a few important results. First of all, the predicted kinetic trap on the stage of $\{Fe(NO)\}^7$ [the complex $(NO^*)H_TH_A$] is indeed the most likely intermediate. Either pathway (1) or (2) would lead to $(NO^*)H_TH_A$. The alternative pathways have prohibitively high barriers. Second, the kinetic trap can be overcome through the PCET $(NO^*)H_TH_A \rightarrow (HNO^-)H_TH_A$. In this case, the activation barrier is only 6.5 kcal/mol and the overall energy of the step is almost thermoneutral. Again, alternative reactions are significantly endothermic and require activation energies higher than 15 kcal/mol. Taken together, it should be noted that the overall scheme is most likely a competition between several pathways, but the most important in the enzymatic catalysis is that both the thermodynamic effects and barriers for the elementary steps are effectively small tractable energies.

2.3. Nitroxyl, Hydroxylamine, and Ammonia Intermediates.

2.3.1. HNO Intermediate. HNO as an intermediate was proposed for several heme-based nitrite and nitric oxide reductases. The interaction of HNO with heme proteins was studied previously by Farmer et al.[113,114] Specifically, HNO bound to heme iron was studied extensively in myoglobin using a variety of experimental methods.[115−117]

The electronic structure of the Fe−HNO complex is exhibited on Figure 9. The σ-bond iron ligand is formed mainly from the metal d_{z^2} orbital. The resulting MO is labeled as d_{z^2}. The other π-bonding MO (labeled d_{yz} in Figure 9) is formed from the ligand p orbital and metal d_{yz}. This is the π-back-bonding interaction with the HNO ligand. The other two metal-based MOs (d_{xy} and d_{xz}) have essentially nonbonding character.

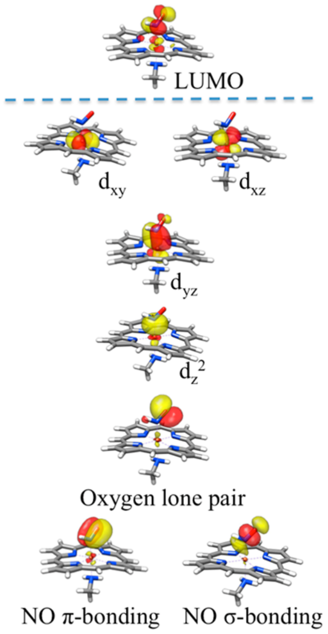

Figure 9. Important MOs for the Fe−HNO complex. The B3LYP/TZV(2d,2p) level of theory was employed. Active-site side chains are omitted for simplicity. The PM algorithm was used to localize the occupied block of the MOs.

The ligand-based MOs are the π and σ bonds between nitrogen and oxygen. Also, there is an oxygen-based lone pair. The lone pair is important for the hydrogen-bonding interactions within the active site as well as for the direction of the electrophilic attack of an incoming proton. The LUMO is mainly a HNO−π* orbital with antibonding character with respect to both the N−O and Fe−N bonds. Orbital analysis concludes that the electronic structure can be viewed as a neutral HNO ligand bound to low-spin Fe^{II}. These results are in agreement with other calculations on coordinated HNO species.[105]

When all possible reactions were analyzed for the Fe−HNO stage,[118] the most probable pathway was found to go through full endothermic protonation of the active site. Importantly, cleavage of the first N−O bond in the NO_2^- substrate in the initial stage of the process is done similarly through endothermic reprotonation of the His_{277} side chain.[97] After reprotonation of the active site, His_{277} acts as the proton donor and an extra electron comes from the neighboring bis-histidine-ligated heme. Two isomeric intermediates, $(HNOH^*)H_TH_A$

and $(H_2NO^*)H_TH_A$, are formed and considered as starting points for the following reaction stage.

2.3.2. Electron Structure and Reactivity on the HNOH and H_2NO Radical Stage. The HNOH and H_2NO radical species are elusive intermediates in the second half-cycle of the nitrite reduction process. Also, HNOH was proposed to be an intermediate in siroheme nitrite reductase[119] and in cytochrome P450 nitrite reductase.[120] Experimentally, HNOH and H_2NO iron porphyrin complexes were characterized by Liu and Ryan.[121]

The electronic structure of $(HNOH^*)H_TH_A$ (Figure 10a) is very similar to that of the Fe−HNO complex. As expected, there are σ and π bonds between nitrogen and oxygen and between iron and N(HNOH) (the d_{z^2}-derived σ interaction and d_{yz} π-back-bonding interaction). The d_{xy} and d_{xz} MOs are nonbonding orbitals. The difference is in the absence of the oxygen lone pair. The extra proton in HNOH interacts with the former oxygen-based lone pair of HNO, and a new bond is formed from the lone-pair electron density. The extra electron enters the SOMO. Here, the SOMO again has an antibonding character with respect to the N−O bond but a bonding character with respect to the Fe−NO bond.

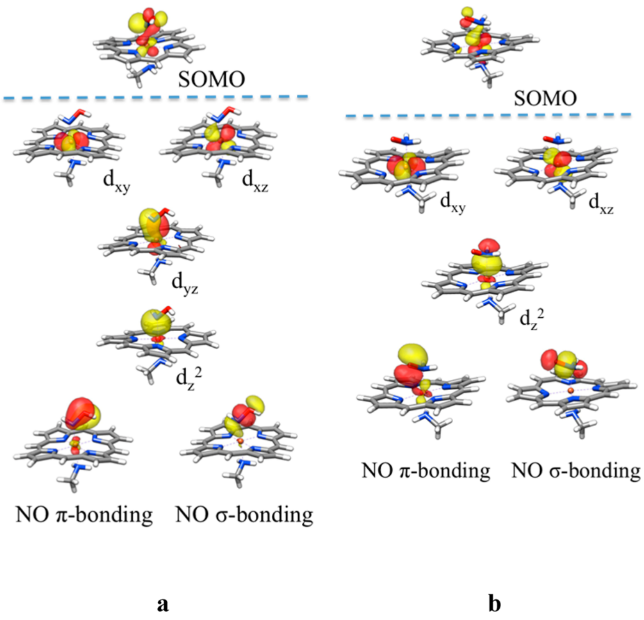

Figure 10. Important PM-localized MOs [B3LYP/TZV(2d,2p)] for $(HNOH^*)H_TH_A$ (a) and $(H_2NO^*)H_TH_A$ (b). Active-site side chains are omitted for simplicity.

The most important feature of the $(H_2NO^*)H_TH_A$ complex is the absence of the additional π-backbonding interaction (compare parts a and b of Figure 10). Obviously, both p orbitals of nitrogen are involved in covalent bonds with two hydrogen atoms, and π-back-donation cannot take place. As a consequence, the Fe−NO bond is very weakened in $(H_2NO^*)H_TH_A$ and elongated to 2.03 Å.

For the $(HNOH^*)H_TH_A$ complex, the spin density is mostly located on the ligand (64%). The situation is completely different for the H_2NO^* core. Here, the spin density is almost exclusively located on iron. Hence, $(HNOH^*)H_TH_A$ is best viewed as a ligand radical bound to low-spin Fe^{II}, whereas $(H_2NO^*)H_TH_A$ is a positive H_2NO^+ core bound to a low-spin Fe^{III} center.

Both $(HNOH^*)H_TH_A$ and $(H_2NO^*)H_TH_A$ complexes were found to be very active. There are a number of possibilities to reach the H_2NOH intermediate. Among them are the following: (a) protonation of $(HNOH^*)H_TH_A$ in an almost thermoneutral step $[(HNOH^*)H_TH_A + H^+ = (H_2NOH^{*+})H_TH_A]$ and a consecutive exothermic reduction $[(H_2NOH^{*+})H_TH_A + e^- = (H_2NOH)H_TH_A]$; (b) exothermic protonation $[(H_2NO^*)H_TH_A + H^+ = (H_2NOH^{*+})H_TH_A]$ and the same reduction to hydroxylamine $[(H_2NOH^{*+})H_TH_A + e^- = (H_2NOH)H_TH_A]$; (c) intramolecular PT from Arg_{114} in the reaction $(H_2NO^*)H_TH_A = (H_2NOH^{*+})H_T$. The last reaction is the most likely scenario because it is the most exothermic among all possibilities and has a very low activation barrier (1.9 kcal/mol). The product of PT from Arg_{114} is then reduced to $(H_2NOH)H_T$ in an exothermic reduction step. Hence, consistent with the experiment, the most likely scenario is the formation of a hydroxylamine intermediate in the form of $(H_2NOH)H_T$ or $(H_2NOH)H_TH_A$.

2.3.3. Hydroxylamine Intermediate and the Second N−O Bond Cleavage. The hydroxylamine intermediate found computationally is also implied as the second half-cycle intermediate by experiments on *Cc*NiR[21,122] and other nitrite reductases.[123,124] Moreover, in the initial work of Einsle et al.,[18] the X-ray structure of the bound hydroxylamine intermediate was solved.

The electronic structure of the hydroxylamine is shown in Figure 11. There is a single N−O σ bond with a distance of 1.46−1.48 Å. The bond distance is very close to the one in free hydroxylamine and thus implies that the electron density redistribution due to binding to heme iron is rather small. Indeed, there are no additional π-back-bonding interactions between iron and hydroxylamine and only one conventional σ-donor coordination-type interaction. All three iron-based MOs, d_{yz}, d_{xz} and d_{xy}, are nonbonding orbitals.

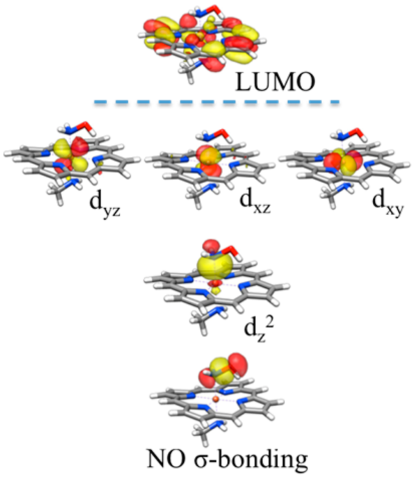

Figure 11. Important MOs [B3LYP/TZV(2d,2p)] for $(H_2NOH)H_TH_A$. Active-site side chains are omitted for simplicity. The PM algorithm was used to localize the occupied MOs.

On the stage of the hydroxylamine intermediate, the second N−O bond is cleaved. It was found that the reaction proceeds through two protonation stages. The protonation of Arg_{114} in the reaction $(H_2NOH)H_T + H^+ = (H_2NOH)H_TH_A$ is highly exothermic, whereas further protonation, leading to $(H_2NOH)H_TH_AH_H$, is slightly endothermic. The fully protonated complex $(H_2NOH)H_TH_AH_H$ then undergoes an intramolecular reaction with His_{277}. As a consequence, a second N−O bond is cleaved and a water molecule is released. Interestingly, the His_{277} amino acid was already implicated to play a key role in the first N−O bond cleavage.[97]

2.3.4. Ammonia Intermediate and Product Dissociation. The ammonia-containing complexes were structurally characterized for the heme-containing enzymes[125,126] as well as for the porphyrin-based synthetic complexes.[127] The electronic structures of the $(H_2N^+)H$ and $(H_2N^*)H$ intermediates are shown in Figure 12. A distinct feature of the $(H_2N^+)H$ compex is strong π-back-bonding interactions. This is indicated by the shape of the d_{yz}-based MO in Figure 12a. The π-back-bonding may be counterproductive for the entire reaction cycle because highly stabile intermediates like the $\{Fe(NO)\}^7$ complex may form and prevent the reaction progress. However, in the case of $(H_2N^+)H_T$, its high electron affinity prevents the reaction from being stalled. The reduction yields −36.2 kcal/mol, and the radical product $(H_2N^*)H_T$ has the other electronic structure (Figure 12b). The Fe−N(H_2N^*) bond is stretched and weakened. The spin density in $(H_2N^*)H_T$ is mostly located on the metal, but the nitrogen atom of the ligand also bears a significant spin. The shape of the SOMO suggests rather delocalized distribution of the unpaired electron (Figure 12b). Importantly, the SOMO is an antibonding MO with respect to the metal−ligand bond and thus is responsible for Fe−N bond weakening.

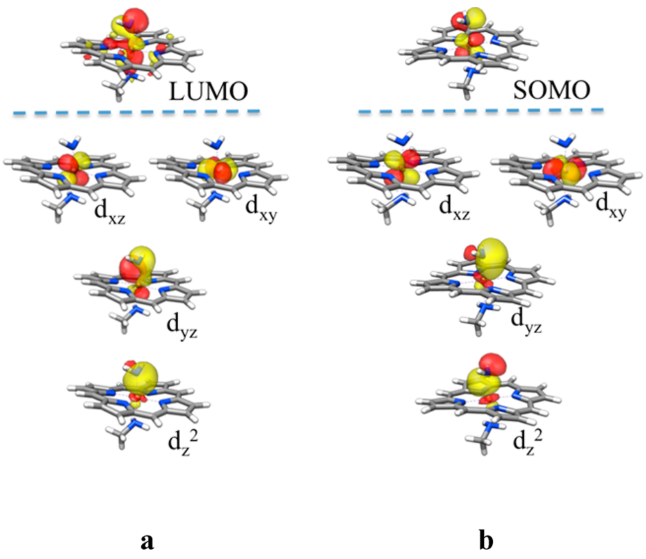

Figure 12. Important MOs [B3LYP/TZV(2d,2p) for $(H_2N^+)H_T$ and $(H_2N^*)H_T$]. PM localization was used for the occupied orbitals. Active-site side chains are omitted for simplicity.

As was already mentioned above, $(H_2N^+)H_T$ is highly electrophilic and abstracts an electron in a highly exothermic reaction: $(H_2N^+)H_T + e^- = (H_2N^*)H_T$. $\Delta G = -36.2$ kcal/mol. $(H_2N^*)H_T$ is also a very active intermediate and readily accepts a proton for Arg_{114}. However, starting from the $(H_2N^*)H_TH_A$ intermediate, there are no further protonations or reductions with a negative driving force. A possibility of intermolecular transfer from Tyr_{218} was studied. Interestingly, Tyr_{218} was shown to be inactive in either ET or PT in the previous stages of the nitrite reduction.[97,111] However, on the present stage, Tyr_{218} was shown to be a competitive proton donor. The barrier of 8 kcal/mol was calculated for the reaction $(H_2N^*)H_TH_A = (H_3N^*)H_A$. Moreover, Tyr_{218} can donate its proton already at the stage of $(H_2N^*)H_T$, before Arg_{114} protonation. In this case, the barrier is even lower and amounts to 5.9 kcal/mol. These findings provide the first theoretical evidence of Tyr_{218}'s possible role in the overall reaction pathway. Importantly, recent electrochemical investigations by Judd et al.[48] also confirm the crucial role of Tyr_{218} in the overall reactivity.

The investigation by Martins et al.[101] provided the first experimental evidence that nitrite binding induces a transition from the high-spin to low-spin configuration of the central iron. In our recent investigation,[118] the dissociation process was studied computationally by performing relaxed surface scans of the Fe−N(NH_3) bond. The goal was to test whether the dissociation takes place on the low- or high-spin potential energy surface. It was found that there is a big difference in the dissociation process depending on the Tyr_{218} protonation state. Specifically, for the complex $(H_3N^*)H_A$, the high- and low-spin energy surfaces never cross. The active-site Fe^{III} stays in the low-spin configuration, and the dissociation energy is more than 13 kcal/mol. The situation is completely different for the $(H_3N^*)H_TH_A$ complex, where Tyr_{218} is protonated. The high-spin surface is now much lower in energy, and thus the low- to high-spin transition may happen. Ammonia is only weakly bound to the high-spin Fe^{III} center and can dissociate easily (the dissociation energy was estimated to be less than 2 kcal/mol). Another nitrite molecule enters the active site, the spin transition to the low-spin configuration happens, and the next catalytic cycle starts. Interesting, similar spin transitions were studied in detail experimentally and with DFT for the synthetic model complexes.[128]

3. DISCUSSION

The six-electron, seven-proton reduction of nitrite to ammonia is a highly complex process. Many factors should work in concert to maintain a high catalytic efficiency and to reach the final product without releasing any intermediates. The most important factors are as follows: (1) substrate activation through specific bonding and back-bonding interactions; (2) well-tuned electron and proton supply chains; (3) the presence of the calcium site active in Lewis acid/base chemistry and proton supply; (4) the presence of Tyr_{218}, which potentially is able to stabilize radical intermediates and is crucial in the late reaction stages; (5) spin-state changes during the reaction, e.g., upon product dissociation. All of these factors turn *Cc*NiR into an extremely interesting subject to study. At the same time, the study needs wide support from a variety of modern computational chemistry methods. In this contribution, we have summarized the reaction mechanism based on our previous investigations on different aspects of the *Cc*NiR reaction cycle.[111,118,97] The most important findings are collected in the scheme in Figure 13.

The catalytic cycle starts from nitrite bound to the low-spin Fe^{II} active site, where all side chains are protonated [the $(NO_2^-)H_TH_AH_H$ complex in Figure 13]. There are two major effects that facilitate substrate activation in the iron(II) nitrite complex: (a) back-bonding and (b) interaction of nitrite with second-sphere residues. As a consequence of the back-bonding effect, the NO_2^--based antibonding LUMO becomes populated and, hence, the N−O bond is weakened. The influence of the interaction of the nitrite oxygen atoms with charged side chains leads to an asymmetric charge distribution that breaks the equivalence of the N−O bonds (both with a formal bond order

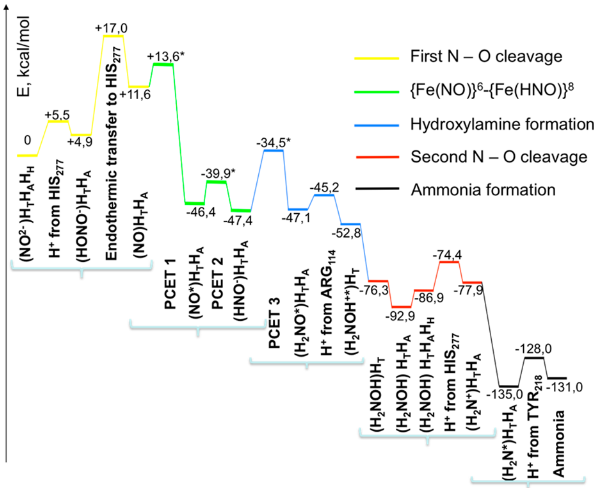

Figure 13. Scheme summarizing the entire nitrite reduction process catalyzed by *Cc*NiR. Transition states denoted with asterisks were estimated using Marcus theory. Only the most plausible reaction pathway is shown.

of 1.5). Hence, the more single bond like the N−O bond is activated for reductive cleavage.

In addition, it was found that the conformation with which the NO_2^- molecule bonds to the active site is optimal for the proton attack from His_{277} and simultaneously for strong back-bonding. Thus, the most acidic side chain in the active site of the *Cc*NiR, His_{277}, is located optimally for carrying out protonation steps. Both features are reflected in the only moderately endothermic reaction energy of +4.9 kcal/mol and the calculated barrier of 5.5 kcal/mol for PT (Figure 13). The $(HONO^-)H_TH_A$ adduct is formed. $(HONO^-)H_TH_A$ represents the lowest conformer with respect to HON═O rotation. Because the rotational potential energy surface is rather rigid, the only feasible way for transfer of the second proton is recharging of His_{277} in this pathway. This can be achieved in a reasonably endothermic step and is rendered irreversible by the barrierless reaction, leading to N−O bond cleavage and formation of the $(NO)H_TH_A$ species. The latter has a $\{Fe(NO)\}^6$ core configuration.

Alternatively, at higher pH, another pathway is considered to be feasible. Above pH ∼ 8, His_{277} is probably in its deprotonated form. Hence, the proton-donor functionality must be adopted by Arg_{114}. Our calculations suggest that this is energetically and kinetically feasible.

Proceeding further from the $\{Fe(NO)\}^6$ species, two scenarios are possible. The most plausible one consists of two consecutive PCET reactions (see PCET1 and PCET2 in Figure 13), and the alternative one is a reduction followed by PCET and protonation. The first pathway is characterized by a highly exothermic first PCET step and almost thermoneutral second PCET step. The calculated free energy difference for the first PCET is −46.2 kcal/mol, and the following second step needs 1 kcal/mol to be accomplished. The second pathway does not contain endothermic reactions and involves only moderately exothermic reactions. In both pathways, the $(HNO^-)H_TH_A$ species is formed.

It should be noted that ET, PT, and PCET events in the active site of *Cc*NiR can only be accomplished through a well-organized network of proton and electron donors. Neighboring low-redox-potential hemes are assumed to be effective electron donors. The change in the reduction state is then immediately accompanied by PT from the inlet channel, part of which is the calcium site. It is this coupling between ET and PT (a characteristic of biological processes), which takes place in the largely hydrophobic interior of proteins, that makes efficient recharging of the active site possible.

Starting from the $(HNO^-)H_TH_A$ species, additionally three electrons and four protons must be provided to reach the final product ammonia. According to our results, the first event is the reduction of the HNO intermediate accomplished by the PCET3 reaction (Figure 13). The intermediate (H_2NO^*)-H_TH_A is formed. This intermediate is highly active and is readily transformed into hydroxylamine most likely through intramolecular PT from Arg_{114} $[(H_2NOH^{+*})H_T]$. The active site then must be reduced and endothermically reprotonated to reach $(H_2NOH)H_TH_AH_H$. Through intermolecular transfer from His_{277}, a heterolytic cleavage reaction of the N−O bond is initiated. As a result, the $(H_2N^+)H_TH_A$ intermediate is formed. The latter readily picks up an electron, forming $(H_2N^*)H_TH_A$, which, in turn, reacts with Tyr_{218}, giving the final product ammonia.

The issue of product dissociation was addressed by conducting relaxed surface scans of the $Fe-N(NH_3)$ distance in two model complexes: $(H_3N^{+*})H_A$ and $(H_3N^{+*})H_TH_A$. It was found that dissociation of the final product ammonia from $(H_3N^{+*})H_A$ is an energy-consuming process. The resonance Raman investigation of Martins et al.[101] provided evidence that the reduction process starts with a transition from the high-spin to the low-spin configuration. This spin-state change was found to take place in dissociation of the product from the $(H_3N^{+*})H_TH_A$ potential energy surface. Here, the elongation of the $Fe-N(NH_3)$ distance leads to switching from the low- to high-energy surface. As a consequence of the spin-state change, dissociation is an overall much less energetically demanding process. According to our results, ammonia is released from the active site in the Fe^{III} state. The open coordination site is then occupied by another nitrite molecule to initiate the next catalytic cycle.

The presented paper unites theoretical efforts in many aspects of the six-electron, seven-proton reduction of nitrite by *Cc*NiR. Using a practical DFT cluster approach extended by the Marcus theory, a number of crucial predictions can be made, for instance, the electronic structure of an intermediate and its influence on the activity, an intermediate steric arrangement, and interaction with the surrounding side chains. Moreover, elementary ET, PT, and PCET stages are considered together with possible sources of the incoming protons and electrons. Intermolecular transition states were allocated. All of this presents a protocol to approach enzymatic catalysis issues with DFT.

■ AUTHOR INFORMATION

Corresponding Authors

*E-mail: dmytro.bykov@gmail.com.
*E-mail: Frank.Neese@cec.mpg.de.

Notes

The authors declare no competing financial interest.

■ ACKNOWLEDGMENTS

We gratefully acknowledge financial support of this work by the Max-Planck Society.

■ REFERENCES

(1) Ye, R. W.; Thomas, S. M. *Curr. Opin. Microbiol.* **2001**, *4*, 307−312.

(2) Jetten, M. S. *Environ. Microbiol.* **2008**, *10*, 2903−9.

(3) Simon, J. *Fems Microbiology Reviews* **2002**, *26*, 285−309.

(4) Richardson, D. J. *Microbiology* **2000**, *146*, 551−571.

(5) Fritz, G.; Einsle, O.; Rudolf, M.; Schiffer, A.; Kroneck, P. M. H. *Journal of Molecular Microbiology and Biotechnology* **2005**, *10*, 223−233.

(6) Bamford, V. A.; Angove, H. C.; Seward, H. E.; Thomson, A. J.; Cole, J. A.; Butt, J. N.; Hemmings, A. M.; Richardson, D. J. *Biochemistry* **2002**, *41*, 2921−2931.

(7) Einsle, O.; Stach, P.; Messerschmidt, A.; Simon, J.; Kroger, A.; Huber, R.; Kroneck, P. M. H. *J. Biol. Chem.* **2000**, *275*, 39608−39616.

(8) Einsle, O.; Messerschmidt, A.; Stach, P.; Bourenkov, G. P.; Bartunik, H. D.; Huber, R.; Kroneck, P. M. H. *Nature* **1999**, *400*, 476−480.

(9) Cunha, C. A.; Macieira, S.; Dias, J. M.; Almeida, G.; Goncalves, L. L.; Costa, C.; Lampreia, J.; Huber, R.; Moura, J. J. G.; Moura, I.; Romao, M. J. *J. Biol. Chem.* **2003**, *278*, 17455−17465.

(10) Almeida, M. G.; Macieira, S.; Goncalves, L. L.; Huber, R.; Cunha, C. A.; Romao, M. J.; Costa, C.; Lampreia, J.; Moura, J. J. G.; Moura, I. *Eur. J. Biochem.* **2003**, *270*, 3904−3915.

(11) Rodrigues, M. L.; Oliveira, T. F.; Pereira, I. A. C.; Archer, M. *EMBO J.* **2006**, *25*, 5951−5960.

(12) Pereira, I. A. C.; LeGall, J.; Xavier, A. V.; Teixeira, M. *Biochim. Biophys. Acta, Protein Struct. Mol. Enzymol.* **2000**, *1481*, 119−130.

(13) Rodrigues, M. L.; Oliveira, T.; Matias, P. M.; Martins, I. C.; Valente, F. M. A.; Pereira, I. A. C.; Archer, M. *Acta Crystallogr., Sect. F: Struct. Biol. Cryst. Commun.* **2006**, *62*, 565−568.

(14) Polyakov, K. M.; Boyko, K. M.; Tikhonova, T. V.; Slutsky, A.; Antipov, A. N.; Zvyagilskaya, R. A.; Popov, A. N.; Bourenkov, G. P.; Lamzin, V. S.; Popov, V. O. *J. Mol. Biol.* **2009**, *389*, 846−862.

(15) Trofimov, A. A.; Polyakov, K. M.; Lazarenko, V. A.; Popov, A. N.; Tikhonova, T. V.; Tikhonov, A. V.; Popov, V. O. *Acta Crystallogr., Sect. D: Biol. Crystallogr.* **2015**, *71*, 1087−94.

(16) Clarke, T. A.; Hemmings, A. M.; Burlat, B.; Butt, J. N.; Cole, J. A.; Richardson, D. J. *Biochem. Soc. Trans.* **2006**, *34*, 143−145.

(17) Burlat, B.; Gwyer, J. D.; Poock, S.; Clarke, T.; Cole, J. A.; Hemmings, A. M.; Cheesman, M. R.; Butt, J. N.; Richardson, D. J. *Biochem. Soc. Trans.* **2005**, *33*, 137−140.

(18) Einsle, O.; Messerschmidt, A.; Huber, R.; Kroneck, P. M. H.; Neese, F. *J. Am. Chem. Soc.* **2002**, *124*, 11737−11745.

(19) Rudolf, M.; Einsle, O.; Neese, F.; Kroneck, P. M. H. *Biochem. Soc. Trans.* **2001**, *30*, 649−653.

(20) Simon, J.; Gross, R.; Einsle, O.; Kroneck, P. M. H.; Kroger, A.; Klimmek, O. *Mol. Microbiol.* **2000**, *35*, 686−696.

(21) Stach, P.; Einsle, O.; Schumacher, W.; Kurun, E.; Kroneck, P. M. H. *J. Inorg. Biochem.* **2000**, *79*, 381−385.

(22) Shinobu, A.; Agmon, N. *J. Phys. Chem. A* **2009**, *113*, 7253−7266.

(23) Goodrich, L. E.; Paulat, F.; Praneeth, V. K. K.; Lehnert, N. *Inorg. Chem.* **2010**, *49*, 6293−6316.

(24) Lehnert, N.; Scheidt, W. R. *Inorg. Chem.* **2010**, *49*, 6223−5.

(25) van Wonderen, J. H.; Burlat, B.; Richardson, D. J.; Cheesman, M. R.; Butt, J. N. *J. Biol. Chem.* **2008**, *283*, 9587−9594.

(26) Enemark, J. H.; Feltham, R. D. *Coord. Chem. Rev.* **1974**, *13*, 339−406.

(27) Roncaroli, F.; Videla, M.; Slep, L. D.; Olabe, J. A. *Coord. Chem. Rev.* **2007**, *251*, 1903−1930.

(28) Wasser, I. M.; de Vries, S.; Moenne-Loccoz, P.; Schroder, I.; Karlin, K. D. *Chem. Rev.* **2002**, *102*, 1201−1234.

(29) Averill, B. A. *Chem. Rev.* **1996**, *96*, 2951−2964.

(30) Scheidt, W. R.; Barabanschikov, A.; Pavlik, J. W.; Silvernail, N. J.; Sage, J. T. *Inorg. Chem.* **2010**, *49*, 6240−52.

(31) Wyllie, G. R. A.; Scheidt, W. R. *Chem. Rev.* **2002**, *102*, 1067−1089.

(32) Nasri, H.; Ellison, M. K.; Shang, M. Y.; Schulz, C. E.; Scheidt, W. R. *Inorg. Chem.* **2004**, *43*, 2932−2942.

(33) Wyllie, G. R.; Silvernail, N. J.; Oliver, A. G.; Schulz, C. E.; Scheidt, W. R. *Inorg. Chem.* **2014**, *53*, 3763−8.

(34) Pavlik, J. W.; Peng, Q.; Silvernail, N. J.; Alp, E. E.; Hu, M. Y.; Zhao, J.; Sage, J. T.; Scheidt, W. R. *Inorg. Chem.* **2014**, *53*, 2582−90.

(35) Lehnert, N.; Sage, J. T.; Silvernail, N.; Scheidt, W. R.; Alp, E. E.; Sturhahn, W.; Zhao, J. *Inorg. Chem.* **2010**, *49*, 7197−215.

(36) Silvernail, N. J.; Pavlik, J. W.; Noll, B. C.; Schulz, C. E.; Scheidt, W. R. *Inorg. Chem.* **2008**, *47*, 912−20.

(37) Silvernail, N. J.; Barabanschikov, A.; Pavlik, J. W.; Noll, B. C.; Zhao, J.; Alp, E. E.; Sturhahn, W.; Sage, J. T.; Scheidt, W. R. *J. Am. Chem. Soc.* **2007**, *129*, 2200−1.

(38) Li, J.; Peng, Q.; Oliver, A. G.; Alp, E. E.; Hu, M. Y.; Zhao, J.; Sage, J. T.; Scheidt, W. R. *J. Am. Chem. Soc.* **2014**, *136*, 18100−10.

(39) Ghosh, A. *Acc. Chem. Res.* **2005**, *38*, 943−54.

(40) Tangen, E.; Svadberg, A.; Ghosh, A. *Inorg. Chem.* **2005**, *44*, 7802−5.

(41) Peng, Q.; Pavlik, J. W.; Scheidt, W. R.; Wiest, O. *J. Chem. Theory Comput.* **2012**, *8*, 214−223.

(42) Almeida, M. G.; Silveira, C. M.; Guigliarelli, B.; Bertrand, P.; Moura, J. J. G.; Moura, I.; Leger, C. *FEBS Lett.* **2007**, *581*, 284−288.

(43) Gwyer, J. D.; Richardson, D. J.; Butt, J. N. *J. Am. Chem. Soc.* **2005**, *127*, 14964−14965.

(44) Marritt, S. J.; Kemp, G. L.; Xiaoe, L.; Durrant, J. R.; Cheesman, M. R.; Butt, J. N. *J. Am. Chem. Soc.* **2008**, *130*, 8588−8589.

(45) Gwyer, J. D.; Angove, H. C.; Richardson, D. J.; Butt, J. N. *Bioelectrochemistry* **2004**, *63*, 43−47.

(46) Mowat, C. G.; Chapman, S. K. *Dalton Transactions* **2005**, 3381−3389.

(47) Lockwood, C. W.; Burlat, B.; Cheesman, M. R.; Kern, M.; Simon, J.; Clarke, T. A.; Richardson, D. J.; Butt, J. N. *J. Am. Chem. Soc.* **2015**, *137*, 3059−68.

(48) Judd, E. T.; Stein, N.; Pacheco, A. A.; Elliott, S. J. *Biochemistry* **2014**, *53*, 5638−46.

(49) Doyle, R. M.; Marritt, S. J.; Gwyer, J. D.; Lowe, T. G.; Tikhonova, T. V.; Popov, V. O.; Cheesman, M. R.; Butt, J. N. *JBIC, J. Biol. Inorg. Chem.* **2013**, *18*, 655−67.

(50) Youngblut, M.; Judd, E. T.; Srajer, V.; Sayyed, B.; Goelzer, T.; Elliott, S. J.; Schmidt, M.; Pacheco, A. A. *JBIC, J. Biol. Inorg. Chem.* **2012**, *17*, 647−62.

(51) Fernandez, M. L.; Estrin, D. A.; Bari, S. E. *J. Inorg. Biochem.* **2008**, *102*, 1523−1530.

(52) Shaw, S.; Lukoyanov, D.; Danyal, K.; Dean, D. R.; Hoffman, B. M.; Seefeldt, L. C. *J. Am. Chem. Soc.* **2014**, *136*, 12776−83.

(53) Steinbach, P. J.; Brooks, B. R. *Proc. Natl. Acad. Sci. U. S. A.* **1993**, *90*, 9135−9139.

(54) Krogan, N. J.; Cagney, G.; Yu, H. Y.; Zhong, G. Q.; Guo, X. H.; Ignatchenko, A.; Li, J.; Pu, S. Y.; Datta, N.; Tikuisis, A. P.; Punna, T.; Peregrin-Alvarez, J. M.; Shales, M.; Zhang, X.; Davey, M.; Robinson, M. D.; Paccanaro, A.; Bray, J. E.; Sheung, A.; Beattie, B.; Richards, D. P.; Canadien, V.; Lalev, A.; Mena, F.; Wong, P.; Starostine, A.; Canete, M. M.; Vlasblom, J.; Wu, S.; Orsi, C.; Collins, S. R.; Chandran, S.; Haw, R.; Rilstone, J. J.; Gandi, K.; Thompson, N. J.; Musso, G.; St Onge, P.; Ghanny, S.; Lam, M. H. Y.; Butland, G.; Altaf-Ul, A. M.; Kanaya, S.; Shilatifard, A.; O'Shea, E.; Weissman, J. S.; Ingles, C. J.; Hughes, T. R.; Parkinson, J.; Gerstein, M.; Wodak, S. J.; Emili, A.; Greenblatt, J. F. *Nature* **2006**, *440*, 637−643.

(55) Neese, F. *J. Inorg. Biochem.* **2003**, *96*, 38−38.

(56) Claeyssens, F.; Harvey, J. N.; Manby, F. R.; Mata, R. A.; Mulholland, A. J.; Ranaghan, K. E.; Schutz, M.; Thiel, S.; Thiel, W.; Werner, H. J. *Angew. Chem., Int. Ed.* **2006**, *45*, 6856−6859.

(57) Jensen, F. *Introduction to Computational Chemistry*; Wiley: New York, 2007.

(58) Neese, F. *JBIC, J. Biol. Inorg. Chem.* **2006**, *11*, 702−711.

(59) Siegbahn, P. E. M.; Blomberg, M. R. A. *Chem. Rev.* **2000**, *100*, 421−437.

(60) Klamt, A.; Schuurmann, G. *J. Chem. Soc., Perkin Trans. 2* **1993**, 799.

(61) Siegbahn, P. E.; Borowski, T. *Faraday Discuss.* **2011**, *148*, 109−17. Discussion 207−28.

(62) Liao, R. Z.; Thiel, W. *J. Comput. Chem.* **2013**, *34*, 2389−97.

(63) Sumowski, C. V.; Ochsenfeld, C. *J. Phys. Chem. A* **2009**, *113*, 11734–41.
(64) Berman, H. M.; Westbrook, J.; Feng, Z.; Gilliland, G.; Bhat, T. N.; Weissig, H.; Shindyalov, I. N.; Bourne, P. E. *Nucleic Acids Res.* **2000**, *28*, 235–242.
(65) Lukat, P.; Rudolf, M.; Stach, P.; Messerschmidt, A.; Kroneck, P. M. H.; Simon, J.; Einsle, O. *Biochemistry* **2008**, *47*, 2080–2086.
(66) Clarke, T. A.; Kemp, G. L.; Van Wonderen, J. H.; Doyle, R.-M. A. S.; Cole, J. A.; Tovell, N.; Cheesman, M. R.; Butt, J. N.; Richardson, D. J.; Hemmings, A. M. *Biochemistry* **2008**, *47*, 3789–3799.
(67) Neese, F. *Wiley Interdisciplinary Reviews-Computational Molecular Science* **2012**, *2*, 73–78.
(68) Perdew, J. P. *Phys. Rev. B: Condens. Matter Mater. Phys.* **1986**, *33*, 8822–8824.
(69) Becke, A. D. *J. Chem. Phys.* **1986**, *84*, 4524–4529.
(70) Neese, F. *J. Comput. Chem.* **2003**, *24*, 1740–1747.
(71) Schafer, A.; Huber, C.; Ahlrichs, R. *J. Chem. Phys.* **1994**, *100*, 5829–5835.
(72) Eichkorn, K.; Treutler, O.; Ohm, H.; Haser, M.; Ahlrichs, R. *Chem. Phys. Lett.* **1995**, *240*, 283–289.
(73) Eichkorn, K.; Weigend, F.; Treutler, O.; Ahlrichs, R. *Theor. Chem. Acc.* **1997**, *97*, 119–124.
(74) Lee, C.; Yang, W.; Parr, R. G. *Phys. Rev. B: Condens. Matter Mater. Phys.* **1988**, *37*, 785.
(75) Becke, A. D. *J. Chem. Phys.* **1993**, *98*, 5648.
(76) Neese, F.; Wennmohs, F.; Hansen, A.; Becker, U. *Chem. Phys.* **2009**, *356*, 98–109.
(77) Ahlrichs, R.; et al., Universität Karlsruhe, Karlsruhe, Germany, 2001; ftp.chemie.uni-karlsruhe.de/pub/basen.
(78) Grimme, S. *J. Comput. Chem.* **2004**, *25*, 1463–1473.
(79) Grimme, S. *J. Comput. Chem.* **2006**, *27*, 1787–1799.
(80) Grimme, S.; Antony, J.; Ehrlich, S.; Krieg, H. *J. Chem. Phys.* **2010**, *132*, 154104.
(81) Weigend, F.; Ahlrichs, R. *Phys. Chem. Chem. Phys.* **2005**, *7*, 3297–305.
(82) Pettersen, E. F.; Goddard, T. D.; Huang, C. C.; Couch, G. S.; Greenblatt, D. M.; Meng, E. C.; Ferrin, T. E. *J. Comput. Chem.* **2004**, *25*, 1605–1612.
(83) Neese, F. *J. Am. Chem. Soc.* **2006**, *128*, 10213–10222.
(84) Pipek, J.; Mezey, P. G. *J. Chem. Phys.* **1989**, *90*, 4916–4926.
(85) Wang, T.; Brudvig, G.; Batista, V. S. *J. Chem. Theory Comput.* **2010**, *6*, 755–760.
(86) Tissandier, M. D.; Cowen, K. A.; Feng, W. Y.; Gundlach, E.; Cohen, M. H.; Earhart, A. D.; Coe, J. V.; Tuttle, T. R. *J. Phys. Chem. A* **1998**, *102*, 7787–7794.
(87) Kelly, C. P.; Cramer, C. J.; Truhlar, D. G. *J. Phys. Chem. B* **2006**, *110*, 16066–16081.
(88) Pace, C. N.; Grimsley, G. R.; Scholtz, J. M. *J. Biol. Chem.* **2009**, *284*, 13285–13289.
(89) Kaila, V. R. I.; Johansson, M. P.; Sundholm, D.; Wikstrom, M. *Proc. Natl. Acad. Sci. U. S. A.* **2010**, *107*, 21470–21475.
(90) Rosso, K. M.; Rustad, J. R. *J. Phys. Chem. A* **2000**, *104*, 6718–6725.
(91) Hatcher, E.; Soudackov, A. V.; Hammes-Schiffer, S. *J. Am. Chem. Soc.* **2004**, *126*, 5763–5775.
(92) Petrenko, T.; Sturhahn, W.; Neese, F. *Hyperfine Interact.* **2007**, *175*, 165–174.
(93) Rydberg, P.; Sigfridsson, E.; Ryde, U. *JBIC, J. Biol. Inorg. Chem.* **2004**, *9*, 203–223.
(94) Goldfarb, D.; Bernardo, M.; Thomann, H.; Kroneck, P. M. H.; Ullrich, V. *J. Am. Chem. Soc.* **1996**, *118*, 2686–2693.
(95) Harvey, J. N. *Principles and Applications of Density Functional Theory in Inorganic Chemistry I* **2004**, *112*, 151–183.
(96) Salomon, O.; Reiher, M.; Hess, B. A. *J. Chem. Phys.* **2002**, *117*, 4729–4737.
(97) Bykov, D.; Neese, F. *JBIC, J. Biol. Inorg. Chem.* **2011**, *16*, 417–430.
(98) Yi, J.; Heinecke, J.; Tan, H.; Ford, P. C.; Richter-Addo, G. B. *J. Am. Chem. Soc.* **2009**, *131*, 18119–18128.
(99) Nasri, H.; Ellison, M. K.; Krebs, C.; Huynh, B. H.; Scheidt, W. R. *J. Am. Chem. Soc.* **2000**, *122*, 10795–10804.
(100) Nasri, H.; Wang, Y. N.; Huynh, B. H.; Walker, F. A.; Scheidt, W. R. *Inorg. Chem.* **1991**, *30*, 1483–1489.
(101) Martins, G.; Rodrigues, L.; Cunha, F. M.; Matos, D.; Hildebrandt, P.; Murgida, D. H.; Pereira, I. A. C.; Todorovic, S. *J. Phys. Chem. B* **2010**, *114*, 5563–5566.
(102) Li, H.; Robertson, A. D.; Jensen, J. H. *Proteins: Struct., Funct., Genet.* **2005**, *61*, 704–721.
(103) Bas, D. C.; Rogers, D. M.; Jensen, J. H. *Proteins: Struct., Funct., Genet.* **2008**, *73*, 765–783.
(104) Olsson, M. H. M.; Søndergaard, C. R.; Rostkowski, M.; Jensen, J. H. *J. Chem. Theory Comput.* **2011**, *7*, 525–537.
(105) Serres, R. G.; Grapperhaus, C. A.; Bothe, E.; Bill, E.; Weyhermuller, T.; Neese, F.; Wieghardt, K. *J. Am. Chem. Soc.* **2004**, *126*, 5138–5153.
(106) Praneeth, V. K. K.; Nather, C.; Peters, G.; Lehnert, N. *Inorg. Chem.* **2006**, *45*, 2795–2811.
(107) Radon, M.; Pierloot, K. *J. Phys. Chem. A* **2008**, *112*, 11824–11832.
(108) Sundararajan, M.; Neese, F. *J. Chem. Theory Comput.* **2012**, *8*, 563–574.
(109) Lehnert, N.; Praneeth, V. K. K.; Paulat, F. *J. Comput. Chem.* **2006**, *27*, 1338–1351.
(110) Xu, C. L.; Spiro, T. G. *JBIC, J. Biol. Inorg. Chem.* **2008**, *13*, 613–621.
(111) Bykov, D.; Neese, F. *JBIC, J. Biol. Inorg. Chem.* **2012**, *17*, 741–760.
(112) Dixon, D. W.; Hong, X.; Woehler, S. E.; Mauk, A. G.; Sishta, B. P. *J. Am. Chem. Soc.* **1990**, *112*, 1082–1088.
(113) Kumar, M. R.; Fukuto, J. M.; Miranda, K. M.; Farmer, P. J. *Inorg. Chem.* **2010**, *49*, 6283–92.
(114) Farmer, P. J.; Sulc, F. *J. Inorg. Biochem.* **2005**, *99*, 166–84.
(115) Lin, R.; Farmer, P. J. *J. Am. Chem. Soc.* **2000**, *122*, 2393–2394.
(116) Zapata, A. L.; Kumar, M. R.; Pervitsky, D.; Farmer, P. J. *J. Inorg. Biochem.* **2013**, *118*, 171–8.
(117) Immoos, C. E.; Sulc, F.; Farmer, P. J.; Czarnecki, K.; Bocian, D. F.; Levina, A.; Aitken, J. B.; Armstrong, R. S.; Lay, P. A. *J. Am. Chem. Soc.* **2005**, *127*, 814–5.
(118) Bykov, D.; Plog, M.; Neese, F. *JBIC, J. Biol. Inorg. Chem.* **2014**, *19*, 97–112.
(119) Farmer, P. J.; Sulc, F. *J. Inorg. Biochem.* **2005**, *99*, 166–184.
(120) Riplinger, C.; Neese, F. *ChemPhysChem* **2011**, *12*, 3192–3203.
(121) Liu, Y. M.; Ryan, M. D. *J. Electroanal. Chem.* **1994**, *368*, 209–219.
(122) Angove, H. C.; Cole, J. A.; Richardson, D. J.; Butt, J. N. *J. Biol. Chem.* **2002**, *277*, 23374–23381.
(123) Hirasawa, M.; Tripathy, J. N.; Sommer, F.; Somasundaram, R.; Chung, J. S.; Nestander, M.; Kruthiventi, M.; Zabet-Moghaddam, M.; Johnson, M. K.; Merchant, S. S.; Allen, J. P.; Knaff, D. B. *Photosynth. Res.* **2010**, *103*, 67–77.
(124) Kuznetsova, S.; Knaff, D. B.; Hirasawa, M.; Setif, P.; Mattioli, T. A. *Biochemistry* **2004**, *43*, 10765–10774.
(125) Roberts, S. A.; Weichsel, A.; Qiu, Y.; Shelnutt, J. A.; Walker, F. A.; Montfort, W. R. *Biochemistry* **2001**, *40*, 11327–11337.
(126) Purwar, N.; McGarry, J. M.; Kostera, J.; Pacheco, A. A.; Schmidt, M. *Biochemistry* **2011**, *50*, 4491–4503.
(127) Kim, Y. O.; Goff, H. M. *Inorg. Chem.* **1990**, *29*, 3907–3908.
(128) Praneeth, V. K.; Paulat, F.; Berto, T. C.; George, S. D.; Nather, C.; Sulok, C. D.; Lehnert, N. *J. Am. Chem. Soc.* **2008**, *130*, 15288–303.